Optimal Orientations of Lithium Niobate for Lateral-and Thickness-Field-Excitation PMUTs

Zhao, Xiaoxi; Pertijs, Michiel; Manzaneque, Tomás

DOI
10.1109/IUS62464.2025.11201595

Publication date
2025

Document Version
Final published version

Published in
2025 IEEE International Ultrasonics Symposium, IUS 2025

Citation (APA)
Zhao, X., Pertijs, M., & Manzaneque, T. (2025). Optimal Orientations of Lithium Niobate for Lateral-and Thickness-Field-Excitation PMUTs. In *2025 IEEE International Ultrasonics Symposium, IUS 2025* (IEEE International Ultrasonics Symposium, IUS). IEEE. https://doi.org/10.1109/IUS62464.2025.11201595

2025 IEEE International Ultrasonics Symposium (IUS) | 979-8-3315-2332-9/25/$31.00 ©2025 IEEE | DOI: 10.1109/IUS62464.2025.11201595

Optimal Orientations of Lithium Niobate for Lateral- and Thickness-Field-Excitation PMUTs

Xiaoxi Zhao, Michiel Pertijs, and Tomás Manzaneque
Email: {x.zhao-4, m.a.p.pertijs, t.manzanequegarcia}@tudelft.nl
Department of Microelectronics, Delft University of Technology
Delft 2628 CD, The Netherlands

***Abstract*—This work identifies the optimal orientation of lithium niobate (LiNbO$_3$, LN) for piezoelectric micromachined ultrasonic transducers (PMUTs) operating in lateral-field excitation (LFE) and thickness-field excitation (TFE) modes. Geometry-independent material figures of merit (FoMs), representing the round-trip signal-to-noise ratio (SNR), are evaluated by sweeping rotated material tensors across the full orientation space. Finite element method (FEM) simulation is then used to quantify the electromechanical coupling k_t^2 under consistent device stacks and electrode layouts. The FoMs peak at 140°Y-cut LiNbO$_3$ (≈120% of PZT-5H); the best commercial TFE option, 128°Y-cut, attains ~65% of that maximum. Under the shared baseline design, the highest k_t^2 is achieved with X-cut LiNbO$_3$ (≈7.2%) using elongated rectangular membranes, about 70% of the PZT-5H reference. Our results provide clear design guidance for LiNbO$_3$ PMUTs to maximize performance: optimal cut, in-plane rotation, and membrane geometry.**

Keywords*—Piezoelectric micromachined ultrasonic transducers (PMUTs), lithium niobate (LiNbO$_3$), lateral field excitation (LFE), thickness field excitation (TFE).

I. INTRODUCTION

Piezoelectric micromachined ultrasonic transducers (PMUTs) have been extensively investigated in recent years due to their key advantages, including the elimination of DC bias requirements, inherently linear responses, and high dynamic deflection ranges [1]. Various PMUT applications, such as medical imaging [2], [3], fingerprint sensing [4], [5], range finding [6], [7] and wireless communication [8], can benefit from these advantages. Recent progress in thin-film piezoelectric materials (e.g., ScAlN, KNN, and LiNbO$_3$) has improved PMUT performance [9], [10], [11]. Among these, LiNbO$_3$ (LN) offers a well-balanced platform for PMUTs due to its low dielectric loss and high piezoelectric coefficients at particular crystallographic orientations.

Thin film LiNbO$_3$ sliced from single-crystal ingots can be cut in various orientations, enabling PMUTs operating in both lateral-field-excitation (LFE) and thickness-field-excitation (TFE) modes. As shown in Fig. 1(a), LFE mode applies an in-plane electric field and induces in-plane mechanical stress, whereas TFE mode applies a through-thickness field to induce in-plane mechanical stress. The device coordinate system defined in Fig. 1 provides a consistent reference: axis 1 is in-plane and initially parallel to the in-plane projection of LiNbO$_3$ polarization direction (Z), axis 2 is orthogonal to axis 1 in the same plane, and axis 3 is out of plane. Because LiNbO$_3$ has anisotropic piezoelectric and elastic tensors, the effective coefficients for bending mode transduction depend on both the cut orientation and the in-plane rotation θ of the device relative to the polarization (Z) axis, as defined in Fig. 1(b).

Previous studies have leveraged specific LiNbO$_3$ orientations for LFE-mode PMUTs, including 36°Y-cut at in-plane rotation of 43° [12], X-cut at 45° [13], 27° [14], and 0° [8]. Despite these investigations, the globally optimal LiNbO$_3$ configurations and orientations for PMUTs remain unclear, and, to our knowledge, no LiNbO$_3$ TFE-mode PMUT has been reported.

To bridge this gap, we map the full LiNbO$_3$ orientation space and identify optimal cuts and in-plane rotations for PMUTs in both operating modes. We first calculate device geometry-independent figures of merit (FoMs) from rotated material tensors, then assess device-level performance with finite-element simulations by extracting the electromechanical coupling factor (k_t^2) under consistent stacks and electrode layouts.

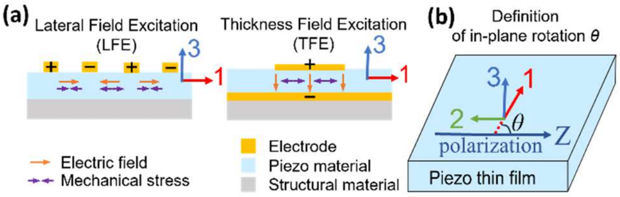

Fig. 1. (a) Operating principles of LFE and TFE modes. (b) Definition of in-plane rotation θ relative to the piezoelectric polarization direction (Z).

II. MATERIAL EVALUATION

A. Method

To evaluate piezoelectric materials for PMUTs independently of device geometry, we adopt the figures of merit (FoMs) outlined in Table I [15]. The transmitting FoM is characterized by the effective piezoelectric coefficient e_{f}, as it is directly proportional to the deflection amplitude of a vibrating membrane. When PMUTs operate as receivers, the signal-to-noise ratio (SNR) is a crucial factor for performance evaluation. Thus, the receiving FoM accounts for maximum SNR in ultrasound reception by incorporating the thermal noise generated from the dielectric losses of the material. This results in the receiving FoM expressed as $e_{\mathrm{f}}/\sqrt{\varepsilon_{\mathrm{f}}\,tan\,\delta}$, where ε_{f} is the effective dielectric constant in the direction of the electric field and $tan\,\delta$ is the dielectric loss tangent. Finally, the transceiving FoM, which quantifies the overall round-trip ultrasonic performance, is given by the product of the transmitting and receiving FoMs.

As shown in Table I, piezoelectric mode-specific effective parameters are used. For LFE mode, we use $e_{11,\mathrm{f}}$ and $\varepsilon_{11,\mathrm{f}}$; for TFE mode, we use $e_{31,\mathrm{f}}$ and $\varepsilon_{33,\mathrm{f}}$. Subscripts follow the coordinate system defined in Fig. 1.

TABLE I. FoMs OF THIN-FILM PMUTs

E-field	Transmitting FoM e_f	Receiving FoM $e_\mathrm{f}/\sqrt{\varepsilon_\mathrm{f}\tan\delta}$	Transceiving FoM $e_\mathrm{f}^2/\sqrt{\varepsilon_\mathrm{f}\tan\delta}$
LFE	$e_{11,\mathrm{f}}$	$e_{11,\mathrm{f}}/\sqrt{\varepsilon_{11,\mathrm{f}}\tan\delta}$	$e_{11,\mathrm{f}}^2/\sqrt{\varepsilon_{11,\mathrm{f}}\tan\delta}$
TFE	$e_{31,\mathrm{f}}$	$e_{31,\mathrm{f}}/\sqrt{\varepsilon_{33,\mathrm{f}}\tan\delta}$	$e_{31,\mathrm{f}}^2/\sqrt{\varepsilon_{33,\mathrm{f}}\tan\delta}$

Our analysis begins by rotating the LiNbO3 material tensors using the Euler-angle rotations following the ZXZ convention. This approach systematically parameterizes arbitrary orientations: a rotation α about the original Z-axis, followed by β about the rotated X-axis, and γ about the rotated Z-axis. With the 3×3 rotation matrix $\mathbf{R}(\alpha, \beta, \gamma)$ and the 6×6 Voigt transformation matrix $\mathbf{M}(\alpha, \beta, \gamma)$, the rotated tensors are:

$$\boldsymbol{\varepsilon}' = \mathbf{R}\boldsymbol{\varepsilon}\,\mathbf{R}^\mathrm{T} \tag{1}$$

$$\mathbf{e}' = \mathbf{R}\mathbf{e}\mathbf{M}^\mathrm{T} \tag{2}$$

$$\mathbf{c}' = \mathbf{M}\mathbf{c}\mathbf{M}^\mathrm{T} \tag{3}$$

where $\boldsymbol{\varepsilon}$, $\mathbf{e}$ and $\mathbf{c}$ are the bulk permittivity, piezoelectric, and stiffness matrices, respectively [16], and primes denote rotated quantities. This framework provides a systematic approach for evaluating any crystallographic cuts and associated in-plane rotations. For instance, $(\alpha, \beta, \gamma) = (90°, 90°, 0°)$ represent X-cut LiNbO3 with zero degree in-plane rotation. From the rotated tensors, we calculate mode-specific effective parameters using the following relations [15], [17]:

$$e_{31,\mathrm{f}} = \frac{d_{31}}{s_{11}^E + s_{12}^E} \tag{4}$$

$$\varepsilon_{33,\mathrm{f}} = \varepsilon_{33}^\sigma - \frac{2d_{31}^2}{(s_{11}^E + s_{12}^E)\varepsilon_0} \tag{5}$$

$$e_{11,\mathrm{f}} = \frac{d_{12}s_{12}^E - d_{11}s_{22}^E}{s_{11}^E s_{22}^E - s_{21}^E s_{12}^E} \tag{6}$$

$$\varepsilon_{11,\mathrm{f}} = \varepsilon_{11}^\sigma + \frac{d_{11}d_{12}(s_{12}^E + s_{21}^E) - d_{11}^2 s_{22}^E - d_{12}^2 s_{11}^E}{(s_{11}^E s_{22}^E - s_{21}^E s_{12}^E)\varepsilon_0} \tag{7}$$

where $\boldsymbol{\varepsilon}^{\boldsymbol{\sigma}}$ is the permittivity at constant stress, $\mathbf{s}^\mathbf{E}$ is the compliance at constant electric field ($\mathbf{s}^\mathbf{E} = \mathbf{c}^{-1}$), $\mathbf{d}$ is the piezoelectric strain tensor ($\mathbf{d} = \mathbf{s}^\mathbf{E} \cdot \mathbf{e}$), and ε_0 is the vacuum permittivity.

B. Material comparison

Using the published bulk properties of commonly used piezoelectric materials [18], we swept the Euler angles across the full orientation space, covering $\alpha \in [-180°, 180°]$, $\beta \in [-90°, 90°]$, and $\gamma \in [-180°, 180°]$. The calculated transceiving FoMs are shown in Fig. 2(a) and (b) for LFE and TFE modes, respectively. The global maximum FoMs were extracted and plotted in Fig. 2(c) and 2(d) for comparison.

For LFE mode, X-cut and 36°Y-cut LiNbO3 closely approach the global maxima at in-plane rotations $\theta \approx 120°$ and 45°/135°, corresponding to $(\alpha, \beta, \gamma) = (90°, 90°, -150°)$ and (0°, 54°, 45°/135°), respectively. For TFE mode, the global maximum occurs near 140°Y-cut at $\theta = 0°/180°$, though this orientation is not commercially available yet; the commercially available 128°Y-cut achieves around 65% of the global maximum at the same θ. Compared to PZT-5H, the best commercially available LiNbO3 orientations reach nearly 50% (X-cut, LFE) and 75 % (128°Y-cut, TFE) of the PZT-5H transceiving FoM.

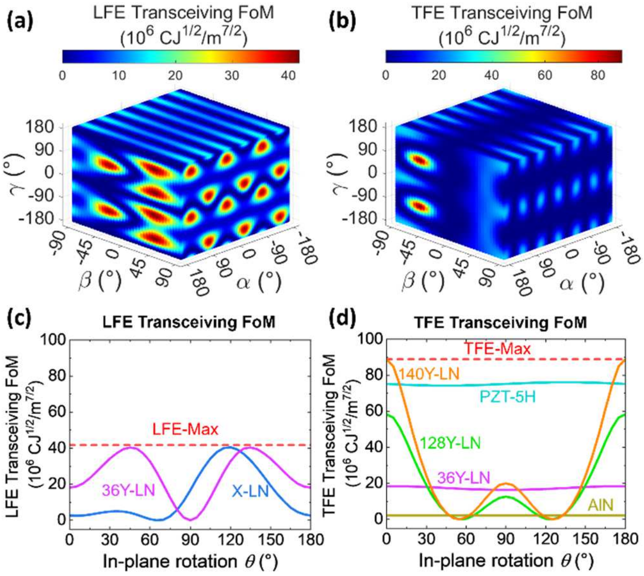

Fig. 2. (a), (b) Transceiving FoMs of all LiNbO3 orientation space for LFE and TFE modes. (c), (d) Extracted maxima and comparison with specific LiNbO3 cuts, PZT and AlN.

III. MODELING AND SIMULATION

A. Simulation settings

Beyond material FoMs, PMUT performance is strongly influenced by device structure. We therefore evaluate the device-level electromechanical coupling factor k_t^2, which quantifies quasi-static electromechanical energy transduction and thus determines the bandwidth of resonant electromechanical systems, e.g. PMUTs. Thus k_t^2 captures the combined effects of piezoelectric coefficients, elasticity, and geometry. From finite element method (FEM) simulation, k_t^2 is extracted via

$$k_t^2 = \frac{\pi^2}{8} \cdot \frac{f_a^2 - f_r^2}{f_r^2} \tag{8}$$

where f_r and f_a are the resonance and anti-resonance frequencies of the PMUT resonator admittance, respectively [19].

As illustrated in Fig. 3(a) and (b), the FEM model used comprises a 1-µm piezoelectric layer and a SiO2 passive layer on a Si substrate; electrodes are modeled with zero thickness. For both LFE and TFE modes, the SiO2 layer thickness ($d_{\mathrm{SiO_2}}$) is swept from 1 to 6 µm; the width of the suspended area is fixed at $W = 80$ µm, while the length L (aspect ratio $AR = L/W$) is varied [Fig. 3(c),(d)]. In LFE mode, the membrane is driven by two pairs of interdigitated electrodes, with the electrode layout tuned to maximize k_t^2. In TFE mode, the bottom electrode fully covers the piezoelectric layer, and the top electrode covers $L/2 \times W/2$ for all aspect ratios. Materials assessed are LiNbO3, PZT-5H, and AlN for TFE mode, and only LiNbO3 for LFE mode (other materials are unsuitable for LFE due to their very small $e_{11,\mathrm{f}}$). The in-plane rotation angle θ is swept to quantify its influence on k_t^2. These settings provides a consistent, albeit not globally optimized, baseline for fairly comparing materials in terms of k_t^2.

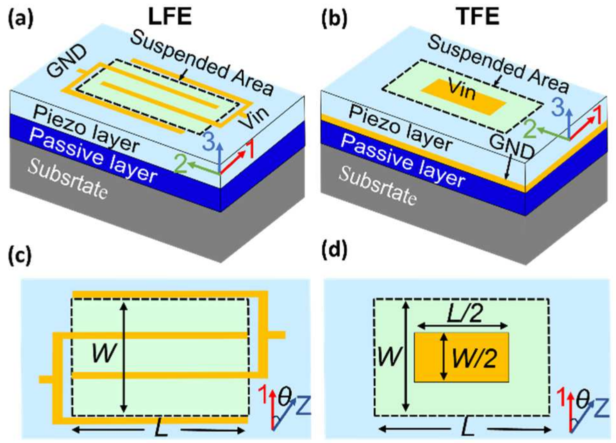

Fig. 3. FEM simulation models for (a) LFE and (b) TFE. (c), (d) Top views with labeled dimension of suspended area. Aspect ratio is defined as $AR = L/W$.

B. *Simulation results and discussion*

First, to isolate the effect of in-plane rotation for LiNbO$_3$, we fixed the passive layer thickness $d_{\mathrm{SiO_2}}$ to 3 μm and the suspended region aspect ratio to $AR = L/W = 4$. As shown in Fig. 4, the trends of k_t^2 with respect to θ is well aligned with the trends of FoMs [Fig. 2(c), (d)] for both LFE and TFE modes: peaks and nulls occur at the same θ. However, the ranking of cuts/materials differs. First, within LFE mode [Fig. 4(a)], 36°Y-cut ($k_t^2 = 5.1\%$) attains around 70% of X-cut despite their similar transceiving FoMs, reflecting the influence of elastic properties captured by k_t^2 but not by the FoMs. Moreover, although the FoMs analysis predicts 140°Y-cut/128°Y-cut (TFE) should outperform X-cut/36°Y-cut (LFE), the FEM simulation yields higher k_t^2 for the LFE cases (e.g., X-cut ≈7.2% vs. 128°Y-cut ≈3.7%). In addition to the elastic properties, this discrepancy may be partly attributed to non-optimized TFE top electrodes coverage.

Next, using LiNbO$_3$ at its optimal in-plane rotations and keeping the $d_{\mathrm{SiO_2}}$ at 3 μm (as in the previous analysis), we evaluated how the aspect ratio AR affects k_t^2. As shown in Fig. 5, LiNbO$_3$ is more suitable to operate in elongated rectangular shape with $AR \geq 4$ for both LFE and TFE modes. By contrast, PZT and AlN peak at $AR = 1$, consistent with their symmetric in-plane piezoelectric coefficients (i.e. $e_{31,f} = e_{32,f}$). At their respective optima, PZT reaches $k_t^2 \approx 10.3\%$, about 1.4 times higher than X-cut LiNbO$_3$; this approximately aligns with the transceiving FoM comparison, where PZT is around 1.8 times X-cut LiNbO$_3$.

Practically, elongated rectangular PMUTs offer advantages over circular elements. At high aspect ratio, the fundamental resonance frequency f_r is dominated primarily by the width (W), decoupling f_r from device area. One can therefore fix f_r via W while increasing active area, and thus sensitivity, by increasing L. In 1D arrays, rectangular elements also simplify pitch/aperture tiling while preserving the target f_r.

Finally, with each material set to its optimal aspect ratio (LiNbO$_3$: $AR = 4$; PZT/AlN: $AR = 1$) and in-plane rotation, we swept the SiO$_2$ thickness $d_{\mathrm{SiO_2}}$ while keeping electrode layouts fixed for fair comparison. As shown in Fig. 6, k_t^2 peaks at different $d_{\mathrm{SiO_2}}$ for each material/cut, determined by the elastic moduli of piezoelectric layer.

The resulting peak values are summarized in Table II: the highest k_t^2 for LiNbO$_3$ is 7.2% achieved with X-cut under LFE mode, which is roughly twice that of 128°Y-cut under TFE mode. Compared to PZT-5H and AlN, X-cut LiNbO$_3$ reaches around 70% of PZT-5H and roughly 10 times AlN. If limited to TFE mode, 128°Y-cut LiNbO$_3$ still achieves around 5 times the k_t^2 of AlN.

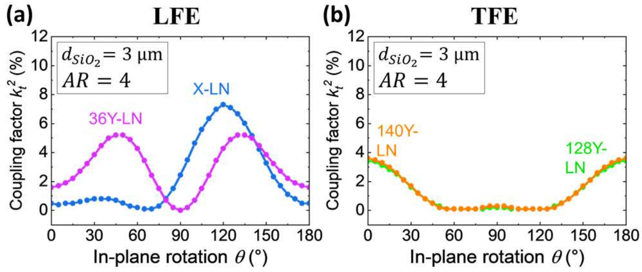

Fig. 4. Simulated k_t^2 for LiNbO$_3$ vs. in-plane rotation θ at fixed d_{SiO_2} and AR: (a) LFE mode; (b) TFE mode.

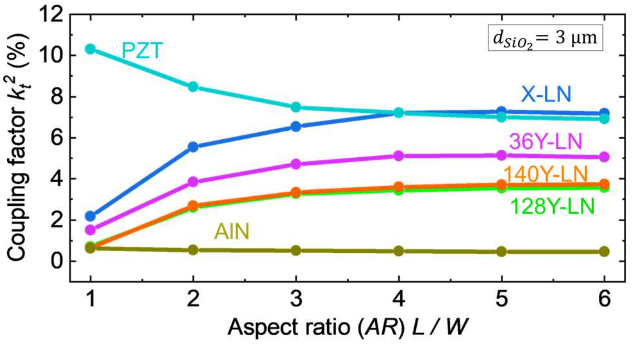

Fig. 5. Simulated k_t^2 vs. aspect ratio of suspended region (AR) at fixed d_{SiO_2}; optimal in-plane rotations is used for each LiNbO$_3$ cut.

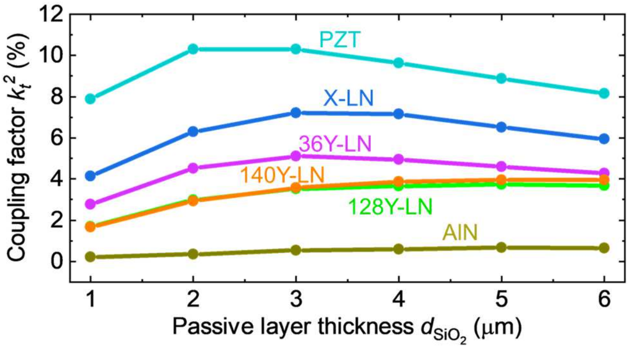

Fig. 6. Simulated k_t^2 vs. d_{SiO_2} with AR and θ fixed at each material's optimum; piezoelectric layer thickness is 1 μm for all cases.

TABLE II. SUMMARY OF PEAK k_t^2 AND OPERATING CONDITIONS

Material	**E-field**	**k_t^2 max**	**θ [°]**	***L/W***	**$d_{\mathrm{SiO_2}}/d_{Piezo}$**
X-LiNbO$_3$	LFE	7.2 %	120°	⩾ 4	3
36°Y-LiNbO$_3$	LFE	5.1 %	45°/135°	⩾ 4	3
140°Y-LiNbO$_3$	TFE	4.0 %	0°/180°	⩾ 4	5
128°Y-LiNbO$_3$	TFE	3.7 %	0°/180°	⩾ 4	5
PZT	TFE	10.3 %	N/A	1	2
AlN	TFE	0.7 %	N/A	1	5

IV. CONCLUSION

In this work, the optimal cuts and device configuration of $LiNbO_3$ for building PMUTs are obtained. The transceiving FoMs across the full orientation space are first evaluated, identifying optimal cuts and in-plane rotations. Device-level FEM simulation confirms the selected $LiNbO_3$ cuts can approach the performance of PZT-based PMUTs. All in all, our results provide practical guidance for making PMUTs with $LiNbO_3$: use X-cut for LFE mode and 128°Y-cut as the best commercial TFE mode option (with 140°Y-cut as a target when available), use elongated rectangular membranes ($AR \geq 4$).

V. REFERENCE

[1] K. Roy, J. E.-Y. Lee, and C. Lee, "Thin-film PMUTs: a review of over 40 years of research," *Microsyst Nanoeng*, vol. 9, no. 1, pp. 1–17, Jul. 2023, doi: 10.1038/s41378-023-00555-7.

[2] Y. Lu, A. Heidari, S. Shelton, A. Guedes, and D. A. Horsley, "High frequency piezoelectric micromachined ultrasonic transducer array for intravascular ultrasound imaging," in *2014 IEEE 27th International Conference on Micro Electro Mechanical Systems (MEMS)*, San Francisco, CA, USA: IEEE, Jan. 2014, pp. 745–748. doi: 10.1109/MEMSYS.2014.6765748.

[3] Z. Liu, S. Yoshida, D. A. Horsley, and S. Tanaka, "Fabrication and characterization of row-column addressed pMUT array with monocrystalline PZT thin film toward creating ultrasonic imager," *Sensors and Actuators A: Physical*, vol. 342, p. 113666, Aug. 2022, doi: 10.1016/j.sna.2022.113666.

[4] Y. Lu *et al.*, "Ultrasonic fingerprint sensor using a piezoelectric micromachined ultrasonic transducer array integrated with complementary metal oxide semiconductor electronics," *Appl. Phys. Lett.*, vol. 106, no. 26, p. 263503, Jun. 2015, doi: 10.1063/1.4922915.

[5] X. Jiang *et al.*, "Monolithic ultrasound fingerprint sensor," *Microsyst Nanoeng*, vol. 3, no. 1, p. 17059, Dec. 2017, doi: 10.1038/micronano.2017.59.

[6] G.-L. Luo, Y. Kusano, and D. A. Horsley, "Airborne Piezoelectric Micromachined Ultrasonic Transducers for Long-Range Detection," *J. Microelectromech. Syst.*, vol. 30, no. 1, pp. 81–89, Feb. 2021, doi: 10.1109/JMEMS.2020.3037298.

[7] D. A. Horsley *et al.*, "Piezoelectric Micromachined Ultrasonic Transducers for Range-Finding Applications," in *2021 5th IEEE Electron Devices Technology & Manufacturing Conference (EDTM)*, Chengdu, China: IEEE, Apr. 2021, pp. 1–3. doi: 10.1109/EDTM50988.2021.9421004.

[8] F. Pop, B. Herrera, and M. Rinaldi, "Lithium Niobate Piezoelectric Micromachined Ultrasonic Transducers for high data-rate intrabody communication," *Nat Commun*, vol. 13, no. 1, p. 1782, Apr. 2022, doi: 10.1038/s41467-022-29355-9.

[9] Q. Wang, Y. Lu, S. Mishin, Y. Oshmyansky, and D. A. Horsley, "Design, Fabrication, and Characterization of Scandium Aluminum Nitride-Based Piezoelectric Micromachined Ultrasonic Transducers," *J. Microelectromech. Syst.*, vol. 26, no. 5, pp. 1132–1139, Oct. 2017, doi: 10.1109/JMEMS.2017.2712101.

[10] L. Zhao, C. Yang, X. Zhang, Z. You, and Y. Lu, "Design, Fabrication, and Characterization of High-Performance PMUT Arrays Based on Potassium Sodium Niobate," *J. Microelectromech. Syst.*, vol. 33, no. 4, pp. 438–445, Aug. 2024, doi: 10.1109/JMEMS.2024.3395294.

[11] X. Zhao, M. Pertijs, and T. Manzaneque, "Piezoelectric Micromachined Ultrasonic Transducer (PMUT) Based on Bilayer X-Cut Lithium Niobate," in *2025 23rd International Conference on Solid-State Sensors, Actuators and Microsystems (Transducers)*, Jun. 2025, pp. 530–533. doi: 10.1109/Transducers61432.2025.11109989.

[12] R. Lu, M. Breen, A. E. Hassanien, Y. Yang, and S. Gong, "A Piezoelectric Micromachined Ultrasonic Transducer Using Thin-Film Lithium Niobate," *J. Microelectromech. Syst.*, vol. 29, no. 6, pp. 1412–1414, Dec. 2020, doi: 10.1109/JMEMS.2020.3026547.

[13] P. Simeoni, Z. Schaffer, and G. Piazza, "A 100 nm Thick, 32 kHz X-Cut Lithium Niobate Piezoelectric Nanoscale Ultrasound Transducer for Airborne Ultrasound Communication," *J. Microelectromech. Syst.*, vol. 30, no. 3, pp. 337–339, Jun. 2021, doi: 10.1109/JMEMS.2021.3062344.

[14] X. Meng *et al.*, "A High Bandwidth PMUT Based on X-Cut Single-Crystal Lithium Niobate for Underwater Communication," *IEEE Sensors J.*, vol. 25, no. 4, pp. 6017–6024, Feb. 2025, doi: 10.1109/JSEN.2024.3507755.

[15] P. Muralt, "Which is the best thin film piezoelectric material?," in *2017 IEEE International Ultrasonics Symposium (IUS)*, 2017, pp. 1–1. doi: 10.1109/ULTSYM.2017.8092065.

[16] J. F. Nye, *Physical Properties of Crystals: Their Representation by Tensors and Matrices*. Oxford university press, 1985.

[17] P. Muralt, "Piezoelectric thin films for MEMS," *Integrated Ferroelectrics*, vol. 17, no. 1–4, pp. 297–307, 1997, doi: 10.1080/10584589708013004.

[18] A. R. Will-Cole *et al.*, "Tutorial: Piezoelectric and magnetoelectric N/MEMS—Materials, devices, and applications," *Journal of Applied Physics*, vol. 131, no. 24, p. 241101, Jun. 2022, doi: 10.1063/5.0094364.

[19] R. Lu, M.-H. Li, Y. Yang, T. Manzaneque, and S. Gong, "Accurate Extraction of Large Electromechanical Coupling in Piezoelectric MEMS Resonators," *J. Microelectromech. Syst.*, vol. 28, no. 2, pp. 209–218, Apr. 2019, doi: 10.1109/JMEMS.2019.2892708.